

Magnetic behavior of $RMn_{2+x}Al_{10-x}$ ($R=La, Gd$) crystals

Athena S. Sefat,^{1,2} Bin Li,^{1,3} Sergey L. Bud'ko,^{1,2} and Paul C. Canfield^{1,2}

¹Ames Laboratory, Ames, Iowa 50011, USA

²Department of Physics and Astronomy, Iowa State University, Ames, Iowa 50011, USA

³Department of Chemistry, Iowa State University, Ames, Iowa 50011, USA

(Received 9 August 2007; published 12 November 2007)

The crystallographic and magnetic properties of the solution grown $RMn_{2+x}Al_{10-x}$ ($R=Gd$ and La) crystals with tetragonal ($P4/nmm$) structure are investigated. For these, single-crystal x-ray diffraction results have shown the preferential occupation of excess manganese on the aluminum $8i$ crystallographic site. Due to excess Mn, there is evidence of local-moment magnetism in $LaMn_{2+x}Al_{10-x}$ and their random distribution is thought to be responsible for the magnetic correlations below ~ 50 K and the spin-glass behavior below ~ 3 K. For $GdMn_{2+x}Al_{10-x}$, the extra manganese influences temperature below which the sample enters into a state with a net ferromagnetic component: $T_C \approx 16$ K for $GdMn_{2.21(4)}Al_{9.79(4)}$ and 25.5 K for $GdMn_{2.39(2)}Al_{9.61(2)}$. Assuming a linear dependence between T_C and excess Mn concentration, the fully stoichiometric and ordered $GdMn_2Al_{10}$ should have $T_C \approx 5$ K.

DOI: 10.1103/PhysRevB.76.174419

PACS number(s): 75.30.Gw, 75.30.Kz, 61.10.-i

I. INTRODUCTION

In the past few decades, binary RMn_{12} (R =rare earth) and ternary R - T -Al systems of RT_4Al_8 and RT_6Al_6 ($T=Cr, Mn, Fe, Co, Ni, Cu$) have attracted interest due to their diverse magnetic phenomena. Among such well-studied aluminides, the properties of RT_2Al_{10} series have not been explored. Within this series, the RMn_2Al_{10} ($R=Y, La-Nd, Sm$, and $Gd-Dy$) and RRe_2Al_{10} ($R=Ce, Pr, Sm$) families crystallize in $CaCr_2Al_{10}$ -structure type ($P4/nmm$).^{1,2} Their tetragonal structure is characterized by two R positions (in Wyckoff notation: $2c, 2a$), one transition-metal position ($8i$), and five Al sites (two $8j, 8i, 8h, 8g$). The R sites are coordinated with four transition metals and 16 Al atoms, with site symmetries of $4mm$ for $R1$ and $-42m$ for $R2$. Each transition-metal atom has two R and ten Al neighbors, and m site symmetry. Because Mn can be nonmagnetic as well as manifest local-moment magnetism,³ RMn_2Al_{10} is the focus of this study.

Numerous measurements have been made on the nonmoment-bearing rare-earth systems of RMn_{12} , RMn_4Al_8 , and RMn_6Al_6 . In YMn_{12} , for example, the moments have been reported as $0.42\mu_B$ for $8i$ and $8j$ sites and $0.14\mu_B$ for $8f$ site.⁴ In $LaMn_4Al_8$ and YMn_4Al_8 , although no magnetic phase transition is seen in the specific heat⁵ and nuclear magnetic resonance results,⁶ muon spin relaxation measurements have indicated the presence of a transition, due to manganese, at ~ 4.5 K.⁷ In $LaMn_4Al_8$, the negative thermal expansion and resistivity upturn found below ~ 40 K have been associated with the development of short-range magnetic correlations.⁸ In $(La_{1-x}Y_x)Mn_4Al_8$, negative thermal expansion was found for $x=0.03$ below ~ 30 K, but not for $x=0.15$.⁹ For the ternary compounds YMn_6Al_6 and $LaMn_6Al_6$, both magnetic and nonmagnetic Mn atoms were observed to coexist.¹⁰ $LaMn_6Al_6$ orders antiferromagnetically below $T_N=4$ K.¹¹ Motivated by such reports, the magnetic properties for $LaMn_{2+x}Al_{10-x}$ will be studied and discussed in this paper.

For the RMn_{12} , RMn_4Al_8 , and RMn_6Al_6 systems with moment-bearing rare earths, numerous interactions and

ground states have been found. For example, in RMn_{12} , the Mn moments couple antiferromagnetically below ~ 100 K, but the rare-earth moments order ferromagnetically below $T_C \sim 10$ K.¹² For members of the RMn_4Al_8 family with $R=Nd, Gd, Tb, Dy$, and Er , there are absences of magnetic order above 1.7, 2, 1.5, 1.7, and 0.5 K, respectively. However, for $PrMn_4Al_8$, a remarkable, antiferromagnetic ordering was found at 14 K.^{5,13-16} For RMn_6Al_6 , $R=Nd$ and Eu have been reported with $T_N=25$ K,¹¹ whereas $R=Gd$ orders below 36 K.¹⁵ Motivated by the diverse properties of these families, two examples of the $GdMn_{2+x}Al_{10-x}$ system, with $x=0.21(4)$ and $0.39(2)$, are investigated here. Presuming RKKY type coupling between the localized $4f$ and the conduction electrons, magnetic interaction between the Gd moments ($J=7/2$) should be the strongest of all $RMn_{2+x}Al_{10-x}$ members, as implied by the deGennes factor $dG=(g_J-1)^2J(J+1)$.¹⁷ In this manner, the investigation of $GdMn_{2+x}Al_{10-x}$ will set a benchmark for the rest of the $RMn_{2+x}Al_{10-x}$ series, similar to other systems.¹⁸⁻²¹

The experimental details below are followed by a discussion of the $RMn_{2+x}Al_{10-x}$ ($R=Gd$ and La) crystal structures and their deviations from stoichiometry. The thermodynamic and transport properties of these materials will then be presented and discussed. The measurements include field- and temperature-dependent magnetizations, specific heat, and electrical resistivity.

II. EXPERIMENTAL DETAILS

Generally, due to high vapor pressure of Mn, the compounds containing it are not easy to synthesize by conventional arc melting, triarc, or optical float zone methods. We have grown $RMn_{2+x}Al_{10-x}$ ($R=La, Gd$) crystals out of an Al-rich self-flux, similar to other growths.²² The procedure involved placing high purity elements ($>3N$) of $R:Mn:Al$ in alumina crucibles, sealing into fused silica tubes under partial argon atmosphere ($\sim \frac{1}{4}$ atm), and heating to $1100^\circ C$, slow cooling ($\sim 5-8^\circ C/h$) to $850^\circ C$, and decanting off the



FIG. 1. (Color online) As grown $\text{GdMn}_{2.21(4)}\text{Al}_{9.79(4)}$ crystal on a millimeter scale paper, depicting typical dimensions of the $\text{RMn}_{2+x}\text{Al}_{10-x}$ crystals and the crystallographic direction.

flux by means of a centrifuge. The solution compositions were $R:\text{Mn}:\text{Al}=1:2:22$ and $1:3:22$. All the crystals were brittle, bar-shaped, and had smooth surfaces. The typical dimensions of crystals were $\sim 1 \times 1 \times 7 \text{ mm}^3$, as shown in Fig. 1.

The initial phase purity and structural identification were made via powder x-ray diffraction, on ground single crystals, using a Rigaku Miniflex x-ray diffractometer ($\text{Cu } K\alpha$ radiation). Subsequent, single-crystal, analyses were made on $\sim \mu\text{m}^3$ crystals with the aid of a STOE image plate x-ray diffractometer ($\text{Mo } K\alpha$ radiation).²³ The data were adjusted for Lorentz and polarization effects, and numerical absorption corrections were done using the X-SHAPE program.²⁴ The structural solutions for all crystals were obtained by the Direct methods²⁵ and refined by full-matrix least-squares re-

finement on F_o^2 using the Bruker SHELXTL 6.1 software package.²⁶ The details of data collection and refinement conditions of $\text{RMn}_{2+x}\text{Al}_{10-x}$ ($R=\text{La}, \text{Gd}$) crystals are given in Table I. In addition, the a and b axes of the crystals were identified. For this, larger samples were glued to a glass capillary and exposed to x rays for 1 min on each frame, collecting data in three runs with nine frames. The indexing and cell reduction were followed by deducing planes. Similar to GdFe_4Al_8 ($I4/mmm$),²⁷ these crystals form with longest side parallel to the c axis.

dc magnetization was measured as a function of temperature $M(T)$ and magnetic field $M(H)$ using a Quantum Design Magnetic Property Measurement System. For a typical temperature sweep experiment, the sample was cooled to 1.8 K in zero-field cooled (zfc) and data were collected by warming from 1.8 to 300 K in an applied field. The sample was then cooled in the applied field cooled (fc), and the measurement repeated from 1.8 K. The notations $\parallel c$ (or $M_{\parallel c}$) and $\perp c$ (or $M_{\perp c}$) denote magnetization measurements made with the applied field, respectively, along and perpendicular to the $[001]$ crystallographic direction.

For temperatures above magnetic ordering, the $M(T)$ data were fitted to a modified Curie-Weiss law where $M/H = \chi = C/(T - \theta) + \chi_0$; C is the Curie constant, θ is the paramagnetic Weiss temperature, and χ_0 is a temperature-independent term which incorporates contributions from Pauli and Van Vleck paramagnetism as well as from core and Landau diamagnetism. The fits to the La compounds were done above 50 K; for the Gd compounds, the fits were done for $T > 150$ K. If the rare earth is the only moment-bearing ion, then the term C is related to the effective moment of the rare-earth ion in paramagnetic state and $\mu_{\text{eff}} = g_L [J(J+1)]^{1/2}$. For Gd^{3+} , $\mu_{\text{eff}} = 7.94 \mu_B$ ($J=7/2$ and $g=2$) and for La^{3+} , $\mu_{\text{eff}}=0$. If manganese is also moment bearing, the additional

TABLE I. Crystal data and structure refinements for $\text{RMn}_{2+x}\text{Al}_{10-x}$ ($R=\text{La}, \text{Gd}$).

Empirical formula	$\text{GdMn}_{2.21(4)}\text{Al}_{9.79(4)}$	$\text{GdMn}_{2.39(2)}\text{Al}_{9.61(2)}$	$\text{LaMn}_{2.26(1)}\text{Al}_{9.74(1)}$	$\text{LaMn}_{2.41(3)}\text{Al}_{9.59(3)}$
Temperature (K)			293(2)	
Wavelength (\AA)			0.71073	
Space group, Z			$P4/nmm, 4$	
Formula weight	542.87	547.76	526.42	530.05
Unit cell dimensions (\AA)	$a=12.760(2)$ $c=5.128(1)$	$a=12.734(2)$ $c=5.127(1)$	$a=12.906(2)$ $c=5.156(1)$	$a=12.889(2)$ $c=5.149(1)$
Volume (\AA^3)	834.8(2)	831.5(2)	858.7(2)	855.3(2)
Density (calculated, g/cm^3)	4.319	4.376	4.068	4.116
Absorption coefficient (mm^{-1})	12.085	12.369	9.066	9.295
Theta range for data collection	$3.19^\circ\text{--}29.96^\circ$	$2.26^\circ\text{--}29.20^\circ$	$3.16^\circ\text{--}30.00^\circ$	$3.16^\circ\text{--}30.08^\circ$
Reflections collected	9622	8287	10576	10320
Independent reflections	650 [$R_{\text{int}}=0.060$]	647 [$R_{\text{int}}=0.042$]	716 [$R_{\text{int}}=0.0583$]	724 [$R_{\text{int}}=0.2785$]
Data/restraints/parameters	650/0/42	647/0/42	716/0/42	724/0/42
Goodness-of-fit on F^2	1.436	1.244	1.395	1.289
Final R indices [$I > 2\sigma(I)$], R_1/wR_2	0.051/0.078	0.032/0.038	0.025/0.044	0.0730/0.138
R indices (all data), R_1/wR_2	0.060/0.081	0.053/0.041	0.027/0.044	0.085/0.146
Largest diff. peak/hole ($e \text{\AA}^{-3}$)	1.902/−2.223	1.341/−1.381	0.893/−0.762	2.640/−2.935

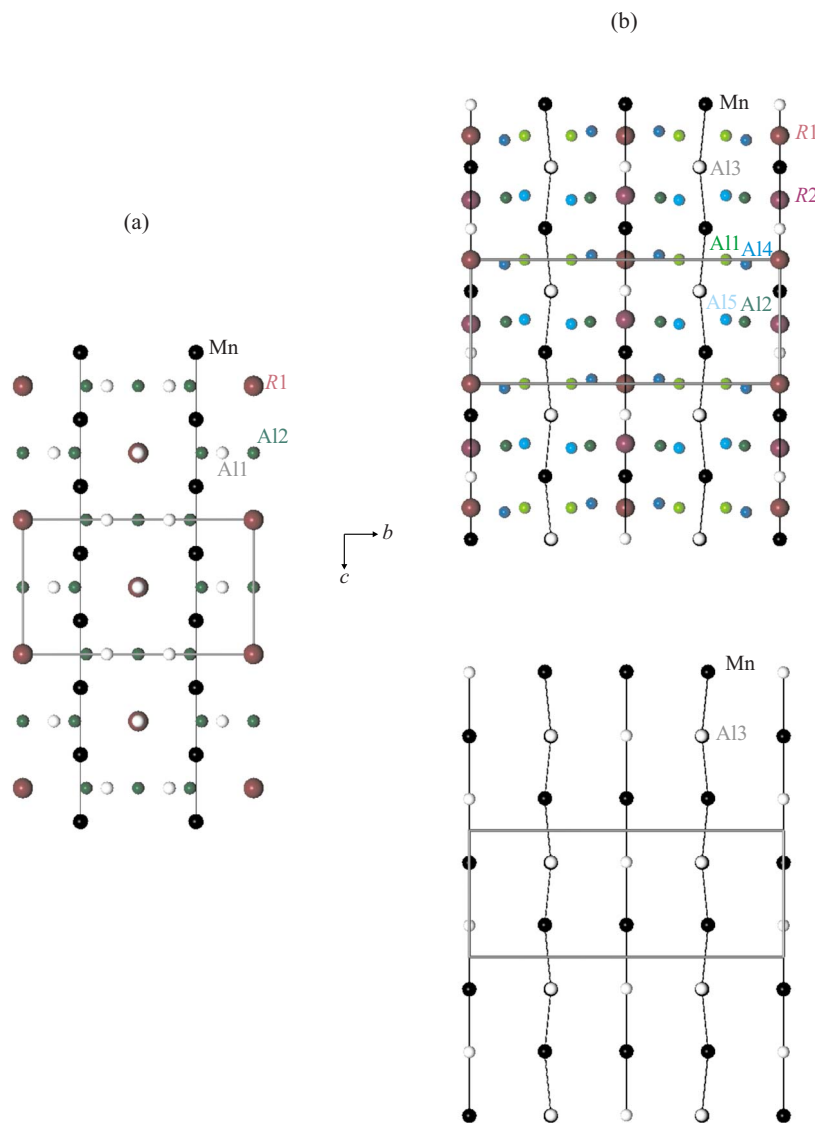


FIG. 2. (Color online) The tetragonal crystal structure of (a) RMn_4Al_8 ($I4/mmm$) with Mn-Mn chains and (b) RMn_2Al_{10} ($P4/nmm$) with Mn-Al3 chains running along the c axis. The bottom of (b) depicts only the Mn and Al3 sublattice (three unit cells along the c axis). Coordination polyhedra in RMn_2Al_{10} are $4mm$ for R1, $-42m$ for R2, and m for Mn.

contributions from Mn^{2+} ($S=5/2$) and Mn^{3+} ($S=2$) are $\mu_{\text{eff}} = 5.92$ and $4.90\mu_B$, respectively.

Specific heat $C_p(T)$ on the single crystals were measured using a Quantum Design Physical Property Measurement System (PPMS) via the relaxation method. The $RMn_{2+x}Al_{10-x}$ samples were measured between 1.8 and 50 K (or in one case up to 75 K). In order to estimate the magnetic specific heat (C_m) for $GdMn_{2+x}Al_{10-x}$ samples, the nonmagnetic contributions above 15 K were approximated by the $LaMn_{2+x}Al_{10-x}$ $C_p(T)$ data. For $T < 15$ K, the nonmagnetic contributions were approximated by an extrapolation of the 15–35 K $LaMn_{2+x}Al_{10-x}$ data using a $C(T) = AT + BT^3$ fit. The magnetic entropies (S) were estimated by integration of C_m/T vs T after an extrapolation of the data down to the origin (i.e., for $T=0$ K, $S=0$) via third order polynomial. The $LaMn_{2.41(3)}Al_{9.59(3)}$ data were used for $GdMn_{2.39(2)}Al_{9.61(2)}$ and that of $LaMn_{2.26(1)}Al_{9.74(1)}$ for $GdMn_{2.21(4)}Al_{9.79(4)}$.

Temperature-dependent electrical resistivity measurements were also performed on the Quantum Design PPMS unit with a 16 Hz excitation current of 3 mA. The electrical contacts were placed on samples in standard four-probe geometry, using Pt wires and silver epoxy (EPO-TEK H20E). The current direction was along the crystallographic c axis for each sample. Residual-resistivity ratios were found from the resistivity $\rho(T)$ data and defined as $RRR = \rho(300 \text{ K})/\rho(1.8 \text{ K})$. It should be noted that vacuum annealing of $R=Gd$ crystals at 500 °C for 48 h did not improve RRR values; therefore, all the data presented here are of the unannealed samples.

III. RESULTS AND DISCUSSION

A. Structure of $RMn_{2+x}Al_{10-x}$ ($R=La, Gd$)

The systematic absences and intensity statistics in all the datasets examined indicated that the structure of

TABLE II. Atomic coordinates and equivalent isotropic displacement parameters ($\text{\AA}^2 \times 10^3$) for $\text{GdMn}_{2.21(4)}\text{Al}_{9.79(4)}$ and $\text{GdMn}_{2.39(2)}\text{Al}_{9.61(2)}$.

Atom	Site	x	y	z	$U(\text{eq})$
$\text{GdMn}_{2.21(4)}\text{Al}_{9.79(4)}$					
Gd1	2c	$\frac{1}{4}$	$\frac{1}{4}$	0.5218(2)	8(1)
Gd2	2a	$\frac{3}{4}$	$\frac{1}{4}$	0	9(1)
Mn	8i	$\frac{1}{4}$	0.5080(1)	0.2507(4)	7(1)
Al1	8j	0.0760(2)	x	0.4818(7)	11(1)
Al2	8j	0.1436(2)	x	0.0286(8)	10(1)
Al3 ^a	8i	$\frac{1}{4}$	0.0084(3)	0.7483(8)	10(1)
Al4	8h	0.3631(2)	$-x$	1/2	10(1)
Al5	8g	0.4254(2)	$-x$	0	12(1)
$\text{GdMn}_{2.39(2)}\text{Al}_{9.61(2)}$					
Gd1	2c	$\frac{1}{4}$	$\frac{1}{4}$	0.5171(1)	8(1)
Gd2	2a	$\frac{3}{4}$	$\frac{1}{4}$	0	9(1)
Mn	8i	$\frac{1}{4}$	0.5068(1)	0.2501(1)	8(1)
Al1	8j	0.0763(1)	x	0.4826(3)	11(1)
Al2	8j	0.1428(2)	x	0.0257(3)	11(1)
Al3 ^b	8i	$\frac{1}{4}$	0.0071(1)	0.7477(3)	8(1)
Al4	8h	0.3623(1)	$-x$	1/2	10(1)
Al5	8g	0.4245(1)	$-x$	0	12(1)

^aAl/Mn=0.91/0.09(2).

^bAl/Mn=0.806/0.194(9).

$\text{RMn}_{2+x}\text{Al}_{10-x}$ ($R=\text{La, Gd}$) is primitive, centrosymmetric, and tetragonal. The crystallographic structure was successfully refined with the known $P4/nmm$ (No. 129) space group.² The structure of $\text{RMn}_2\text{Al}_{10}$ may be derived from the binary ThMn_{12} type which crystallizes in $I4/mmm$ space group. In this body centered structure, the 2a positions are occupied by Th (i.e., atoms of lanthanides or actinides) and manganese atoms are located on the three eightfold sites (in Wyckoff notation 8i, 8j, and 8f).⁴ When a third element, e.g., Al is added, as in the case of RMn_4Al_8 ,²⁸ a superstructure of the ThMn_{12} -type results in which the Mn atoms occupy only one of the three positions (8f) and the two other nonequivalent positions are fully occupied by aluminum.²⁹ Figure 2(a) presents RMn_4Al_8 structure where Mn atoms form linear chains along the c axis. There are two sets of Mn-Mn bond distances: the intrachain (along c axis) of 2.5–2.6 \AA and the interchain distances of 4.4–4.5 \AA .³⁰ In the $\text{RMn}_2\text{Al}_{10}$ crystal structure, the unit cell volume is doubled due to the ordered arrangement of manganese and aluminum atoms on what has been the manganese 8f site of RMn_4Al_8 [Fig. 2(b)]. In $\text{RMn}_2\text{Al}_{10}$, the transition-metal atoms form linear chains made alternately of Al (on the Al3 site) and Mn along the c axis with shortest Mn-Mn (interchain) distances of ~ 4.5 \AA [Fig. 2(b), bottom].

The data refinement of the $\text{RMn}_2\text{Al}_{10}$ compositions ($R=\text{La, Gd}$) provided eight peaks of which two were assigned to Gd, one to Mn, and five to Al atoms according to peak intensities. A few (~ 5) least-squares cycles followed by a difference Fourier map revealed that Al3 site was too electron rich to be occupied by aluminum alone and it gave

smaller displacement parameter compared to other four Al sites. Allowing mixtures of aluminum and manganese on the Al3 site gave more reasonable isotropic displacement parameters with improvements in R_1 as well as lower difference peaks. The refinements with free occupancies of the other four Al sites show that each of them is close to unity within 3σ and as a result, they were fixed in later refinement cycles. The final refinement with anisotropic displacement parameters and a secondary extinction correction, converged to the R values listed in Table I. Previous studies of compounds with ThMn_{12} structure type have reported disorder among the 8f, 8i, and 8j sites.³¹ Similarly, the $\text{RMn}_2\text{Al}_{10}$ structure refinements gave slight disorder. Tables II and III give the corresponding atomic positions, isotropic-equivalent displacement parameters, and site occupancies of $\text{RMn}_{2+x}\text{Al}_{10-x}$ with $R=\text{Gd}$ and La. Based on these analyses, we find that an initial solution composition of $R:\text{Mn}:\text{Al}=1:2:22$ yields single crystals of $\text{GdMn}_{2.21(4)}\text{Al}_{9.79(4)}$ and $\text{LaMn}_{2.26(1)}\text{Al}_{9.74(1)}$ stoichiometries, whereas $R:\text{Mn}:\text{Al}=1:3:22$ yields single crystals of $\text{GdMn}_{2.39(2)}\text{Al}_{9.61(2)}$ and $\text{LaMn}_{2.41(3)}\text{Al}_{9.59(3)}$. For these four compositions, selected interatomic distances are given in Table IV. Although for the stoichiometric $\text{RMn}_2\text{Al}_{10}$ the shortest Mn-Mn distances are the interchain distances [Fig. 2(b)], for $\text{RMn}_{2+x}\text{Al}_{10-x}$, because of the excess distribution of Mn preferentially on Al3 sites, shorter intrachain Mn-Mn distances (labeled as Mn-Mn3 in Table IV) are also found. By introducing Mn on the Al3 site, the electronic environments around the R1 and R2 atoms are modified by introducing shorter R1-Mn3 (compared to R1-Mn) and longer R2-Mn3 (compared to R2-Mn) distances.

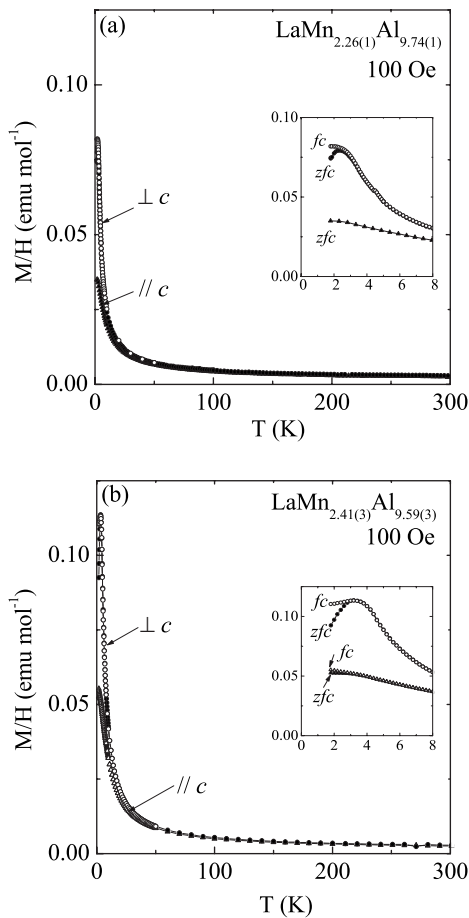


FIG. 3. Temperature dependence of magnetization in zero-field-cooled (zfc) and field-cooled (fc) forms along two crystallographic directions for (a) $\text{LaMn}_{2.26(1)}\text{Al}_{9.74(1)}$ and (b) $\text{LaMn}_{2.41(3)}\text{Al}_{9.59(3)}$. Insets are the low-temperature regions.

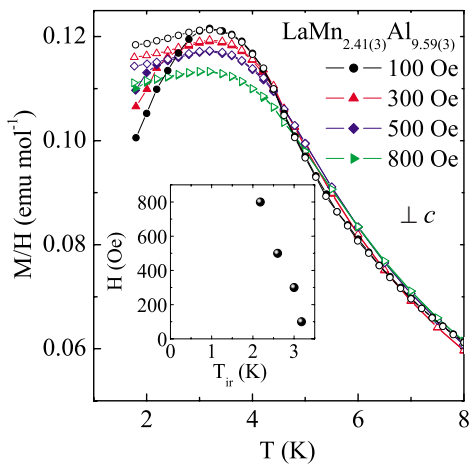


FIG. 4. (Color online) For $\text{LaMn}_{2.41(3)}\text{Al}_{9.59(3)}$, the zero field-cooled (zfc) and field-cooled (fc) magnetization results vs temperature at chosen applied fields along the easy axis of magnetization, $M_{\perp c}$. The inset is a plot of magnetic field vs the irreversibility temperature (T_{ir}) found at zfc/fc separation curves.

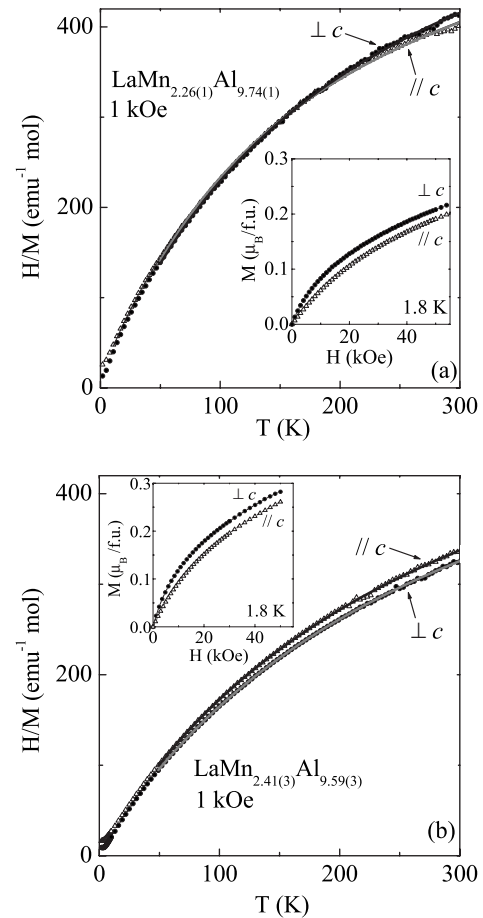


FIG. 5. Along the two crystallographic directions and for (a) $\text{LaMn}_{2.26(1)}\text{Al}_{9.74(1)}$ and (b) $\text{LaMn}_{2.41(3)}\text{Al}_{9.59(3)}$, the plots of inverse magnetization with fits to modified Curie-Weiss above 50 K. The insets are the field-dependent magnetization results at 1.8 K.

B. Physical properties

1. $\text{LaMn}_{2+x}\text{Al}_{10-x}$

The temperature-dependent magnetization, at 100 Oe, for the $\text{LaMn}_{2.26(1)}\text{Al}_{9.74(1)}$ and $\text{LaMn}_{2.41(3)}\text{Al}_{9.59(3)}$ crystals is found to be positive and rapidly increasing with decreasing temperature below ~ 50 K (Fig. 3). The magnetization is anisotropic at these low temperatures with $M_{\perp c} \sim 2M_{\parallel c}$ at 2 K. For each measured crystal direction, the value of magnetization at 1.8 K is lower for $\text{LaMn}_{2.26(1)}\text{Al}_{9.74(1)}$ [Fig. 3(a)] than for $\text{LaMn}_{2.41(3)}\text{Al}_{9.59(3)}$ [Fig. 3(b)]. The results for $M_{\perp c}$ clearly separate into zfc and fc branches at low temperatures (Fig. 3, insets). Such irreversible behavior suggests either a ferromagnetic component or a spin-glass freezing.³² For $M_{\perp c}$, there are peaklike features in zfc data as opposed to featureless plateaus in the fc data below a $T_{\text{ir}} = 2.8$ K and 3.2 K for $\text{LaMn}_{2.26(1)}\text{Al}_{9.74(1)}$ and $\text{LaMn}_{2.41(3)}\text{Al}_{9.59(3)}$, respectively. Such low field irreversibility and anisotropy is characteristic of a spin glass and is similar to $\text{Y}_{1-x}\text{Tb}_x\text{Ni}_2\text{Ge}_2$ system for low concentration of terbium, below $x \sim 0.35$.³³ With higher applied fields, the zfc $M_{\perp c}$ curve becomes more rounded, shifting the zfc/fc separation to lower temperatures.

TABLE III. Atomic coordinates and equivalent isotropic displacement parameters ($\text{\AA}^2 \times 10^3$) for $\text{LaMn}_{2.26(1)}\text{Al}_{9.74(1)}$ and $\text{LaMn}_{2.41(3)}\text{Al}_{9.59(3)}$.

Atom	Site	x	y	z	$U(\text{eq})$
$\text{LaMn}_{2.26(1)}\text{Al}_{9.74(1)}$					
La1	2c	$\frac{1}{4}$	$\frac{1}{4}$	0.5205(1)	8(1)
La2	2a	$\frac{3}{4}$	$\frac{1}{4}$	0	9(1)
Mn	8i	$\frac{1}{4}$	0.5068(1)	0.2533(1)	8(1)
Al1	8j	0.0750(1)	x	0.4856(2)	12(1)
Al2	8j	0.1401(1)	x	0.0288(2)	11(1)
Al3 ^a	8i	$\frac{1}{4}$	0.0066(1)	0.7517(2)	9(1)
Al4	8h	0.3642(1)	$-x$	1/2	11(1)
Al5	8g	0.4259(1)	$-x$	0	11(1)
$\text{LaMn}_{2.41(3)}\text{Al}_{9.59(3)}$					
La1	2c	$\frac{1}{4}$	$\frac{1}{4}$	0.5187(2)	7(1)
La2	2a	$\frac{3}{4}$	$\frac{1}{4}$	0	8(1)
Mn	8i	$\frac{1}{4}$	0.5062(1)	0.2525(1)	8(1)
Al1	8j	0.0755(1)	x	0.4865(2)	12(1)
Al2	8j	0.1398(1)	x	0.0258(2)	11(1)
Al3 ^b	8i	$\frac{1}{4}$	0.0057(1)	0.7510(2)	8(1)
Al4	8h	0.3644(1)	$-x$	1/2	10(1)
Al5	8g	0.4256(1)	$-x$	0	11(1)

^aAl/Mn=0.870(6)/0.130(6).^bAl/Mn=0.795/0.205(15).

This is shown for $\text{LaMn}_{2.41(3)}\text{Al}_{9.59(3)}$ in Fig. 4; the applied magnetic fields are plotted as a function of T_{ir} in the inset. For fields above 800 Oe, the irreversibility drops below 1.8 K.

The high temperature magnetization results of $\text{LaMn}_{2+x}\text{Al}_{10-x}$ crystals, measured in applied field of 1 kOe, are essentially isotropic. Above 50 K, the inverse of magnetization data were fitted to a modified Curie-Weiss temperature dependence (Fig. 5). The inferred Weiss temperatures for both La samples are approximately zero, indicating weak exchange interactions between Mn ions (Table V). The interpretation of the effective moment, μ_{eff} , may be made per

formula unit (Table V), or per each Mn assuming that all Mn atoms in the unit formula contribute equally to the total magnetic moment, or per excess Mn on Al3 sites assuming that only the x contributes to the local-moment magnetism. For $\text{LaMn}_{2.26(1)}\text{Al}_{9.74(1)}$ $\mu_{\text{eff}} \approx 1.5\mu_B/\text{f.u.}$, or $0.7\mu_B/\text{Mn}$, or $5.8\mu_B/x\text{Mn}$ ($x=0.26$). For $\text{LaMn}_{2.41(3)}\text{Al}_{9.59(3)}$ $\mu_{\text{eff}} \approx 1.9\mu_B/\text{f.u.}$, $0.8\mu_B/\text{Mn}$, or $4.6\mu_B/x\text{Mn}$ ($x=0.41$). The effective moment per formula unit is slightly larger for the sample with higher manganese concentration. Although the experimental $\mu_{\text{eff}}/\text{Mn}$ are exceptionally low, the $\mu_{\text{eff}}/x\text{Mn}$ are close to the expected spin-only theoretical values of $5.92\mu_B/\text{Mn}^{2+}$ and $4.90\mu_B/\text{Mn}^{3+}$. This strongly suggests that

TABLE IV. Selected bond lengths (\AA) for $\text{RMn}_{2+x}\text{Al}_{10-x}$ ($R=\text{La, Gd}$). The percentages of bonds involving manganese partial occupancy of Al3 site (Mn3).

Bond	$\text{GdMn}_{2.21(4)}\text{Al}_{9.79(4)}$	$\text{GdMn}_{2.39(2)}\text{Al}_{9.61(2)}$	$\text{LaMn}_{2.26(1)}\text{Al}_{9.74(1)}$	$\text{LaMn}_{2.41(3)}\text{Al}_{9.59(3)}$
R1-Mn	3.574(2)	3.545(1)	3.5894(6)	3.575(1)
R2-Mn	3.344(2)	3.352(1)	3.3993(6)	3.400(1)
R1-Mn3	3.294(3) ^a	3.311(2) ^b	3.3596(9) ^c	3.369(2) ^d
R2-Mn3	3.541(3) ^a	3.520(2) ^b	3.5506(9) ^c	3.536(2) ^d
Mn-Mn	4.518(3)	4.507(2)	4.5627(9)	4.553(2)
Mn-Mn3	2.585(5), 2.560(5) ^a	2.582(3), 2.558(3) ^b	2.592(1), 2.575(1) ^c	2.587(2), 2.571(2) ^d

^a9(2)%.^b19(1)%.^c13(1)%.^d21(2)%.

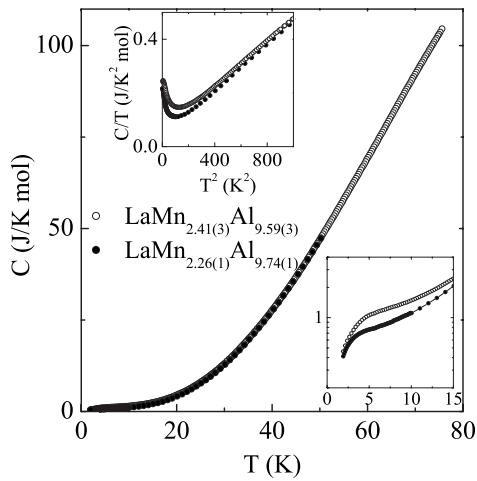


FIG. 6. For $\text{LaMn}_{2.26(1)}\text{Al}_{9.74(1)}$ and $\text{LaMn}_{2.41(3)}\text{Al}_{9.59(3)}$, the temperature dependence of specific heat. The insets are the enlarged low-temperature region (bottom) and the data in the form of C/T vs T^2 (top).

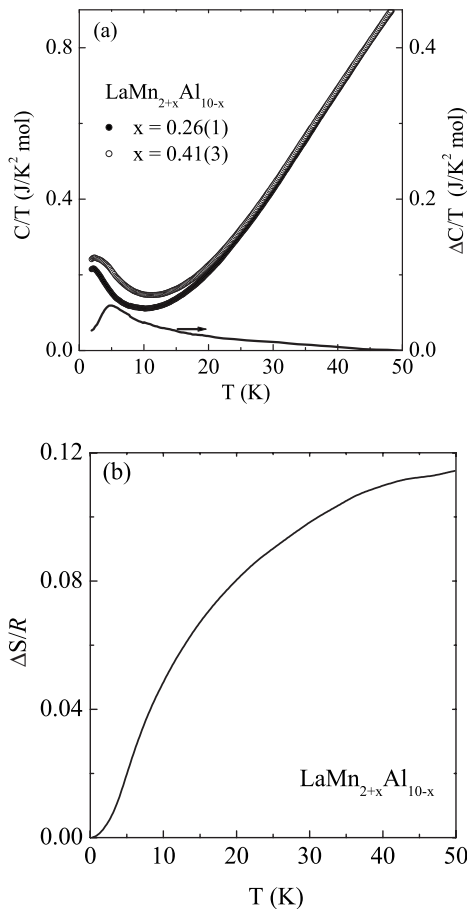


FIG. 7. For $\text{LaMn}_{2.26(1)}\text{Al}_{9.74(1)}$ and $\text{LaMn}_{2.41(3)}\text{Al}_{9.59(3)}$, (a) specific heat in the form of C/T vs T , along with the difference in the two data ($\Delta C/T$), (b) the difference in entropy between the two samples ($\Delta S/R$).

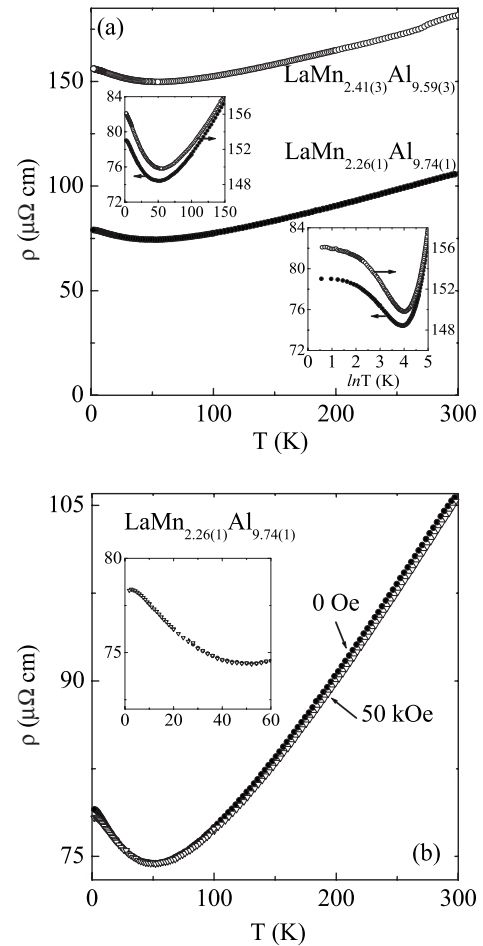


FIG. 8. (a) For $\text{LaMn}_{2.26(1)}\text{Al}_{9.74(1)}$ and $\text{LaMn}_{2.41(3)}\text{Al}_{9.59(3)}$, the temperature dependence of electrical resistivity at zero applied field. The insets represent the enlarged low-temperature regions (top) and also the ρ vs $\ln T$ (bottom). (b) The temperature dependence of resistivity for $\text{LaMn}_{2.26(1)}\text{Al}_{9.74(1)}$ at 0 Oe and 50 kOe applied fields, with the inset representing the enlarged low-temperature regions.

the magnetic behavior found in the $\text{LaMn}_{2+x}\text{Al}_{10-x}$ compounds is due to the localized moment-bearing Mn on the Al3 site, although we do not claim to be able to distinguish between the two possible valence values.

Field-dependent magnetization isotherms along the two crystallographic axes for $\text{LaMn}_{2+x}\text{Al}_{10-x}$ are shown as insets of Fig. 5, measured at 1.8 K. Neither sample approaches a saturated value at the highest field measured. As a result, the magnetization at ~ 55 kOe attains $\sim 0.21\mu_B/\text{f.u.}$ ($0.09\mu_B/\text{Mn}$ or $0.81\mu_B/x\text{Mn}$) for $\text{LaMn}_{2.26(1)}\text{Al}_{9.74(1)}$ and $\sim 0.27\mu_B/\text{f.u.}$ ($0.11\mu_B/\text{Mn}$ or $0.66\mu_B/x\text{Mn}$) for $\text{LaMn}_{2.41(3)}\text{Al}_{9.59(3)}$, all of which are far below the expected free ion magnetic moment values: $4\mu_B/\text{Mn}^{3+}$ and $5\mu_B/\text{Mn}^{2+}$.

The temperature dependences of specific heat for $\text{LaMn}_{2+x}\text{Al}_{10-x}$ crystals are shown in Fig. 6. Whereas $C(T)$ increases monotonically over the whole temperature range, low-temperature upturns, $T < 10$ K, are found in the C/T vs T^2 data (top inset). These data, taken together with the low-

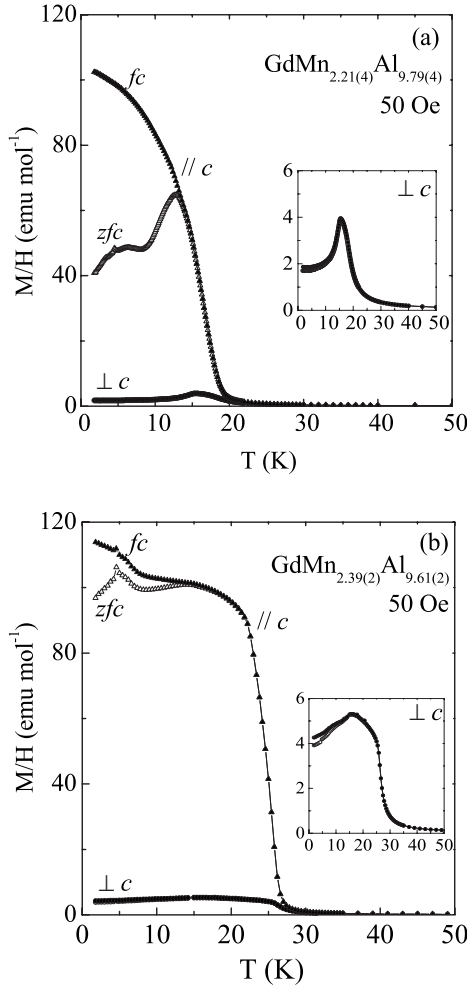


FIG. 9. Temperature dependence of magnetization in zero field-cooled (zfc) and field-cooled (fc) forms for (a) $\text{GdMn}_{2.21(4)}\text{Al}_{9.79(4)}$ and (b) $\text{GdMn}_{2.39(2)}\text{Al}_{9.61(2)}$, along two crystallographic directions.

temperature, low field magnetization data shown in Fig. 3, are inconsistent with ferromagnetic order but are suggestive of spin-glass formation.

The estimates of magnetic specific heat in $\text{LaMn}_{2+x}\text{Al}_{10-x}$ are made difficult by the lack of a nonmagnetic $C_p(T)$ background. The temperature dependence of specific heat for the two La samples in the form of C/T and $\Delta C/T$ (ΔC

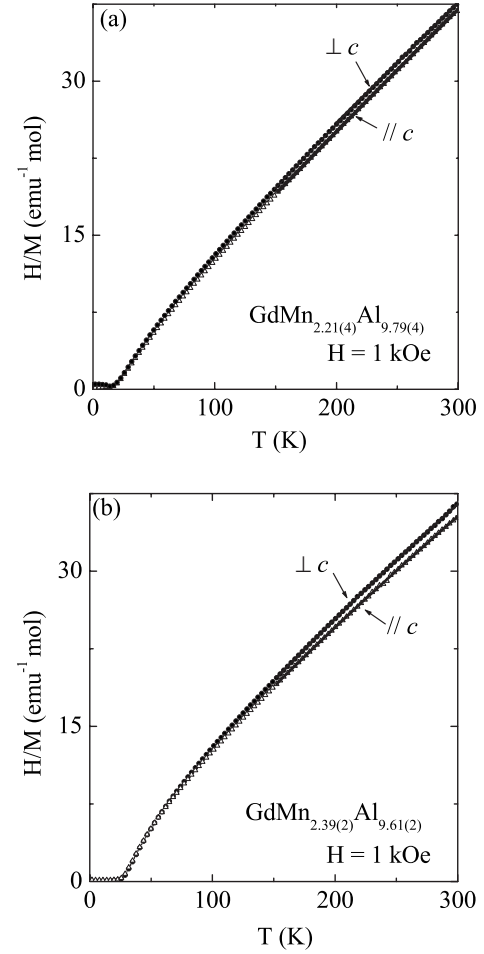


FIG. 10. The inverse of temperature-dependent magnetization (1 kOe) and the fits above 150 K to Curie-Weiss for (a) $\text{GdMn}_{2.21(4)}\text{Al}_{9.79(4)}$ and (b) $\text{GdMn}_{2.39(2)}\text{Al}_{9.61(2)}$.

$= C_{x=0.41} - C_{x=0.26}$) is shown in Fig. 7(a). Since $\Delta C/T$ is finite up to ~ 45 K, the attempts to model accurate γ and β from a $C(T) = \gamma T + \beta T^3$ were not possible. However, in order to consider Mn local moment on Al3 sites, the specific heat data of the sample with the smaller x were used as background for the sample with larger x . The change in entropy between the two samples resulting from the differences in magnetic contributions is shown in Fig. 7(b). For 0.15(3) manganese difference (as estimated from x-ray refinement), the entropy S

TABLE V. For samples with $\text{RMn}_{2+x}\text{Al}_{10-x}$ ($R=\text{La, Gd}$), the critical ordering temperature (T_C), paramagnetic Weiss temperature (θ), paramagnetic effective moment (μ_{eff}) and temperature independent term (χ_0) are listed.

	$\sim T_C$ (K)	θ (K)		μ_{eff} ($\mu_B/\text{f.u.}$)		χ_0 (emu mol^{-1})	
		$\parallel c$	$\perp c$	$\parallel c$	$\perp c$	$\parallel c$	$\perp c$
$\text{LaMn}_{2.26(1)}\text{Al}_{9.74(1)}$	—	2(1)	-1(1)	1.5(2)	1.5(1)	0.0016(1)	0.0014(1)
$\text{LaMn}_{2.41(3)}\text{Al}_{9.59(3)}$	—	-2(1)	-2(2)	1.9(2)	1.9(1)	0.0015(1)	0.0016(1)
$\text{GdMn}_{2.21(4)}\text{Al}_{9.79(4)}$	16	-4(2)	-0(1)	8.0(2)	7.9(2)	0.0010(1)	0.0020(1)
$\text{GdMn}_{2.39(2)}\text{Al}_{9.61(2)}$	25.5	0(3)	-2(1)	7.7(2)	7.5(2)	0.0036(4)	0.0030(3)

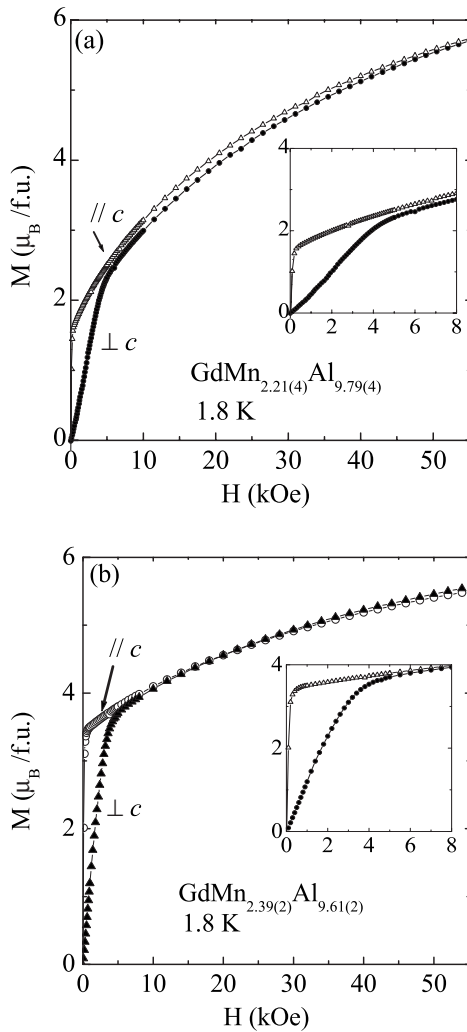


FIG. 11. Magnetization vs applied field of (a) $\text{GdMn}_{2.21(4)}\text{Al}_{9.79(4)}$ and (b) $\text{GdMn}_{2.39(2)}\text{Al}_{9.61(2)}$, along two different crystallographic axes, at 1.8 K. The insets are the low field regions.

$\sim 0.11R$ up to ~ 45 K implies $0.8(2)R$ per Mn. This value may suggest a doublet ground state ($R \ln 2 \approx 0.69R$). However, assuming no crystalline electric field effects, as the theoretical entropy is $1.8R/\text{Mn}^{2+}$ ($\ln 6$) and $1.6R/\text{Mn}^{3+}$ ($\ln 5$), this value is essentially within a factor of 2 of the expected entropy and is consistent with local manganese moment.

The $\rho(T)$ results for the $\text{LaMn}_{2+x}\text{Al}_{10-x}$ samples are dominated by large residual resistivities that probably originate from the noted atomic disorder in the crystals [Fig. 8(a)]. For $\text{LaMn}_{2.41(3)}\text{Al}_{9.59(3)}$, $\rho_{1.8\text{ K}}$ ($155 \mu\Omega \text{ cm}$) is nearly twice that of $\text{LaMn}_{2.26(1)}\text{Al}_{9.74(1)}$ ($80 \mu\Omega \text{ cm}$). The residual-resistivity ratios (RRRs) are 1.2 and 1.3, respectively. Three distinct regions are observed in the resistivity vs temperature curves. At high temperatures, the resistivity decreases with decreasing temperature. This decrease is mainly due to electron-phonon scattering processes. For $\text{LaMn}_{2.26(1)}\text{Al}_{9.74(1)}$ and $\text{LaMn}_{2.41(3)}\text{Al}_{9.59(3)}$, the resistivity minima are seen at ~ 50 and 55 K, respectively [Fig. 8(a), top inset]. Below, the rise in ρ data is possibly related to the development of magnetic correlations. Similar minima in $\rho(T)$ have also been found in

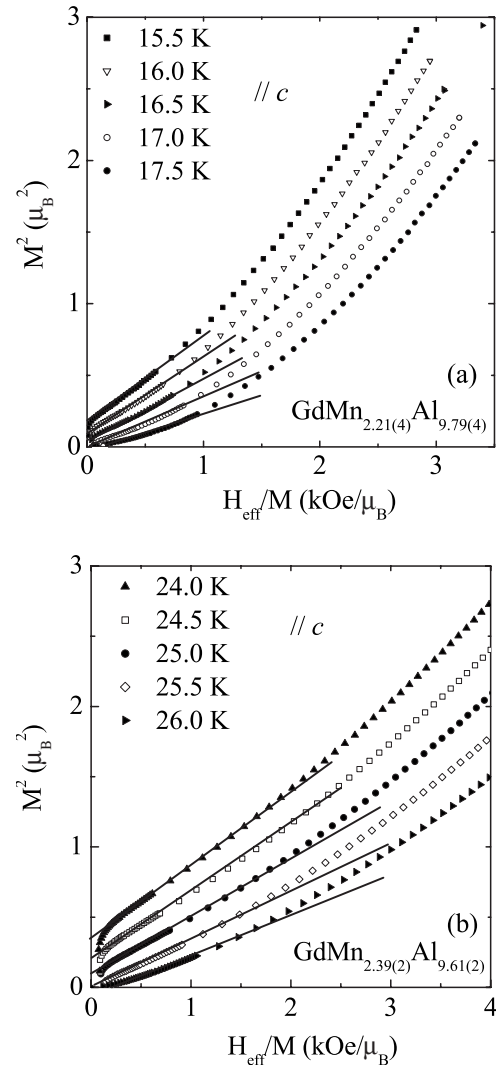


FIG. 12. The Arrott plots in the form of M^2 vs H_{eff}/M for $M_{\parallel c}$ and (a) $\text{GdMn}_{2.21(4)}\text{Al}_{9.79(4)}$ and (b) $\text{GdMn}_{2.39(2)}\text{Al}_{9.61(2)}$, where H_{eff} is the effective field estimates acting in each sample.

LaMn_4Al_8 at ~ 40 K (Ref. 8) and YMn_6Al_6 at ~ 25 K.³⁴ Upon the application of 50 kOe [Fig. 8(b)], there is a slight change of high temperature resistivity slope, shown for $\text{LaMn}_{2.26(1)}\text{Al}_{9.74(1)}$, perhaps due to localization of spins. With applied magnetic field, it is likely that there is a reduction of the spin-disorder scattering due to an increase of the polarization of the magnetic moments.³⁵ The small negative magnetoresistivity especially below ~ 10 K is noteworthy [Fig. 8(b), inset].

On the whole then, $C(T)$, $M(T, H)$, and $\rho(T)$ data are consistent with the formation of a low-temperature spin-glass state, formed from local-moment Mn located on the Al3 sites which are disordered due to the mixed occupancy of Mn and Al. Although the $\text{LaMn}_{2+x}\text{Al}_{10-x}$ samples show local-moment behavior, the random distribution of the magnetic manganese atoms can be responsible for the frustration of ordering and the spin-glass freezing. The resistivity minimum and the rise in magnetization in each sample below ~ 50 K can be attributed to the development of magnetic correlations giving rise to the spin-glass phase below T_{ir} . Whereas a resistivity mini-

imum could also be an indication of the Kondo effect arising from the strong magnetic impurity screening,³⁶ the $\rho(T)$ results do not fit the logarithmic behavior of $\rho_K \alpha \ln T$ (Ref. 37) [Fig. 8(a), bottom inset], and the T_{ir} features in $M(T)$ are not inherently associated with Kondo screening.

2. $\text{GdMn}_{2+x}\text{Al}_{10-x}$

The temperature dependence of magnetization in 50 Oe for $\text{GdMn}_{2+x}\text{Al}_{10-x}$ crystals is shown in Fig. 9. The $M(T)$ results along both crystallographic directions of $M_{\parallel c}$ and $M_{\perp c}$ separate into zfc and fc branches. At low temperatures and fields, $M_{\parallel c} \gg M_{\perp c}$. The magnetization for $\text{GdMn}_{2.21(4)}\text{Al}_{9.79(4)}$ increases below ~ 20 K [Fig. 9(a)] and for $\text{GdMn}_{2.39(2)}\text{Al}_{9.61(2)}$ this rise is more steep and occurs below ~ 28 K [Fig. 9(b)]. For these, the irreversibility in zfc/fc temperatures are ~ 13 and ~ 15 K, respectively, each with a small zfc anomaly in $M_{\parallel c}$ at 4.6 K.

The magnetization data for each $\text{GdMn}_{2+x}\text{Al}_{10-x}$ composition, measured in an applied field of 1 kOe, are plotted as H/M in Fig. 10. The $M(T)$ results are essentially isotropic in the paramagnetic state. The Weiss temperatures and paramagnetic moments are summarized in Table V. For $\text{GdMn}_{2+x}\text{Al}_{10-x}$ compositions, the derived μ_{eff} values are close to that expected for Gd^{3+} free ion ($7.94\mu_B$).

Field-dependent magnetization data at 1.8 K are shown in Fig. 11. The applied field of 55 kOe is insufficient to saturate the magnetization data which is still well below the $7\mu_B$ associated with Gd^{3+} . For both $\text{GdMn}_{2+x}\text{Al}_{10-x}$ crystals, the $M_{\perp c}$ and $M_{\parallel c}$ are essentially isotropic above ~ 5 kOe. The $M_{\parallel c}$ rises rapidly up to ~ 400 Oe and changes weakly thereafter. In comparison, $M_{\perp c}$ rises more slowly at smaller fields to 5 kOe, and follows $M_{\parallel c}$ curve thereon (Fig. 11, insets). The precipitous rise in magnetization at low fields along c as well as the noted zfc/fc hysteresis indicate that there is a ferromagnetic component to the ordered state in Gd samples.

In order to locate the ferromagnetic transition temperature for each $\text{GdMn}_{2+x}\text{Al}_{10-x}$ composition, magnetization isotherms in the vicinity of Curie temperatures have been measured for $M_{\parallel c}$ and for the construction of Arrott plots³⁸ in the form of M^2 vs $H_{\text{eff}}M^{-1}$ (Fig. 12). H_{eff} estimates the effective field inside the sample and is found by subtracting the demagnetizing field H_d by applied field ($H_d = NM$, where N is the demagnetizing factor dependent on sample shape). Demagnetization corrections of $0.10 \text{ kOe}/\mu_B$ and $0.08 \text{ kOe}/\mu_B$ were used for $\text{GdMn}_{2.21(4)}\text{Al}_{9.79(4)}$ and $\text{GdMn}_{2.39(2)}\text{Al}_{9.61(2)}$, respectively ($N \approx 0.20$). For $\text{GdMn}_{2.21(4)}\text{Al}_{9.79(4)}$, $16 \text{ K} < T_C < 17 \text{ K}$ and for $\text{GdMn}_{2.39(2)}\text{Al}_{9.61(2)}$, $25 \text{ K} < T_C < 26 \text{ K}$ (Fig. 12). As will be discussed below, these values are consistent with the anomalies in C_p data. It should be noted though, that since the transition in each sample may not be purely ferromagnetic in nature, the formal use of Arrott analysis may be questionable.

The transition to long-range magnetic order can be seen in zero-field specific heat results, displayed in Fig. 13. $\text{GdMn}_{2.21(4)}\text{Al}_{9.79(4)}$ and $\text{GdMn}_{2.39(2)}\text{Al}_{9.61(2)}$ samples manifest anomalies at ~ 16 K and ~ 25.5 K, respectively. In similar systems, magnetic order shifts from 2 K in GdMn_4Al_8 to

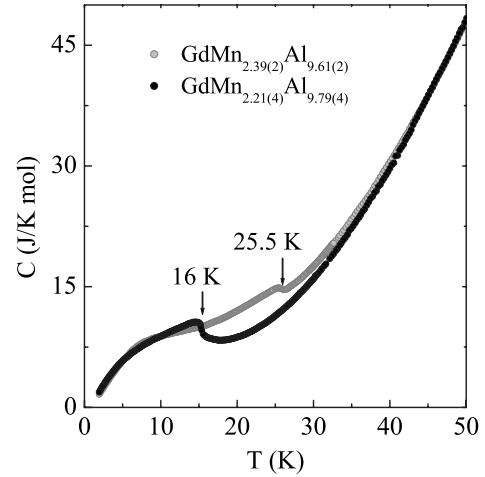


FIG. 13. Temperature dependence of specific heat for $\text{GdMn}_{2.21(4)}\text{Al}_{9.79(4)}$ and $\text{GdMn}_{2.39(2)}\text{Al}_{9.61(2)}$.

36 K in GdMn_6Al_6 .¹⁵ The magnetic specific heat results (C_m) are depicted in Fig. 14 along with magnetic entropy S/R . The eight-fold ground states [for Gd^{3+} $J=7/2$, $R \ln 8 \approx 2.08R$] are approximately recovered for both of $\text{GdMn}_{2+x}\text{Al}_{10-x}$ compositions.

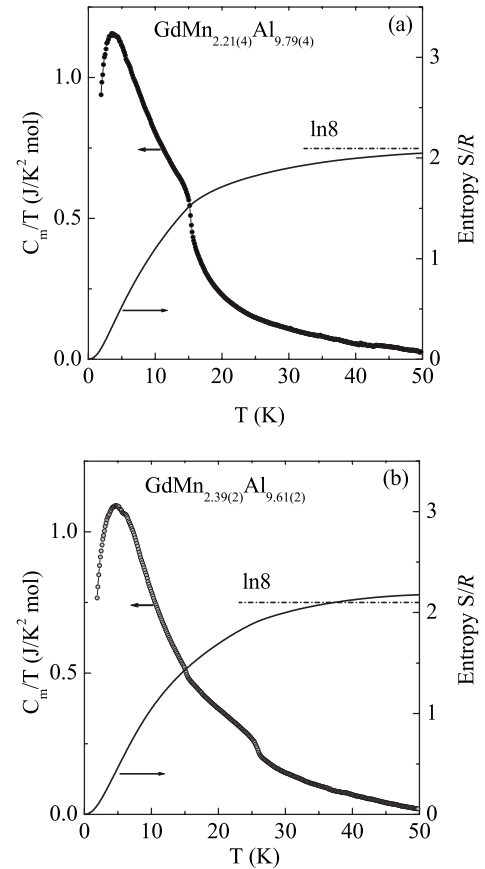


FIG. 14. Temperature dependence of magnetic specific heat in the form of C_m/T and entropy change (S/R) for (a) $\text{GdMn}_{2.21(4)}\text{Al}_{9.79(4)}$ and (b) $\text{GdMn}_{2.39(2)}\text{Al}_{9.61(2)}$.

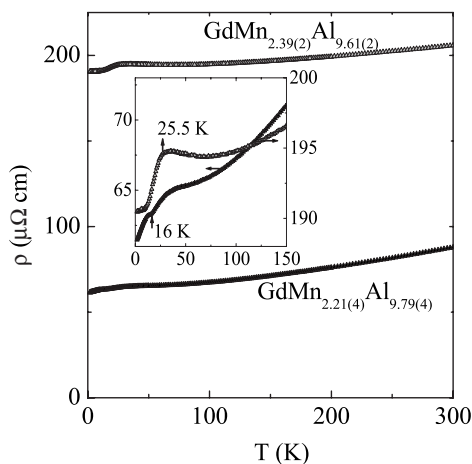


FIG. 15. Temperature dependence of electrical resistivity for $GdMn_{2.21(4)}Al_{9.79(4)}$ and $GdMn_{2.39(2)}Al_{9.61(2)}$. The inset is the enlarged low-temperature data, with shifted ρ scales.

The temperature dependent electrical resistivity data for the Gd samples are shown in Fig. 15. The RRR for $GdMn_{2.21(4)}Al_{9.79(4)}$ is 1.4 ($\rho_{1.8\text{ K}} \approx 60 \mu\Omega\text{ cm}$) and even lower for the more structurally disordered $GdMn_{2.39(2)}Al_{9.61(2)}$: $RRR \sim 1.1$ ($\rho_{1.8\text{ K}} \approx 190 \mu\Omega\text{ cm}$). For $GdMn_{2.39(2)}Al_{9.61(2)}$, ρ manifests a drop below 25.5 K (inset), consistent with a decrease of magnetic scattering in the ordered state. For $GdMn_{2.21(4)}Al_{9.79(4)}$, there is a kink at 16 K, similar to that reported for $GdMn_{12}$ ($RRR \sim 1.2$).³⁹

IV. CONCLUSIONS

RMn_2Al_{10} ($R=La$ or Gd) solution grown crystals form with full R crystallographic site occupancies ($2c$ and $2a$), Mn ($8i$), and five Al sites (two $8j$, $8i$, $8h$, $8g$). However, dependent on the initial melt composition, various amounts of extra manganese are accommodated on the $Al3$ ($8i$) site (Tables II and III). In $RMn_{2+x}Al_{10-x}$, the excess Mn introduces short intrachain Mn-Mn bonds [Fig. 2(b)], modifying the electronic environments around $R1$ and $R2$ atoms by shorter $R1$ -Mn and longer $R2$ -Mn distances (Table IV).

For the $LaMn_{2+x}Al_{10-x}$ samples, higher Mn concentrations lead to increased local-moment magnetism as found by higher magnitude of magnetization value (Fig. 3, insets), larger specific heat anomaly (Fig. 6, bottom inset), and slightly higher temperature upturn in resistivity [Fig. 8(a), top inset]. However, $LaMn_{2.41(3)}Al_{9.59(3)}$ sample has higher chemical disorder compared to $LaMn_{2.26(2)}Al_{9.84(2)}$, giving lower RRR and higher $\rho_{1.8\text{ K}}$ [Fig. 8(a)]. Structurally for $LaMn_{2.26(2)}Al_{9.84(2)}$, there are 13(1)% Mn-Mn intrachain distances with 2.584(1) Å averaged length due to excess Mn on $Al3$ site; for $LaMn_{2.41(3)}Al_{9.59(3)}$, there are 21(2)% of 2.579(3) Å intrachain Mn-Mn bonds. The critical nearest Mn-Mn interatomic distance of ~ 2.7 Å has been found to dominate the stability of the Mn moment in intermetallic compounds of RMn_2 , for example. For these, the larger unit cell volume results in narrower $3d$ bandwidth and higher

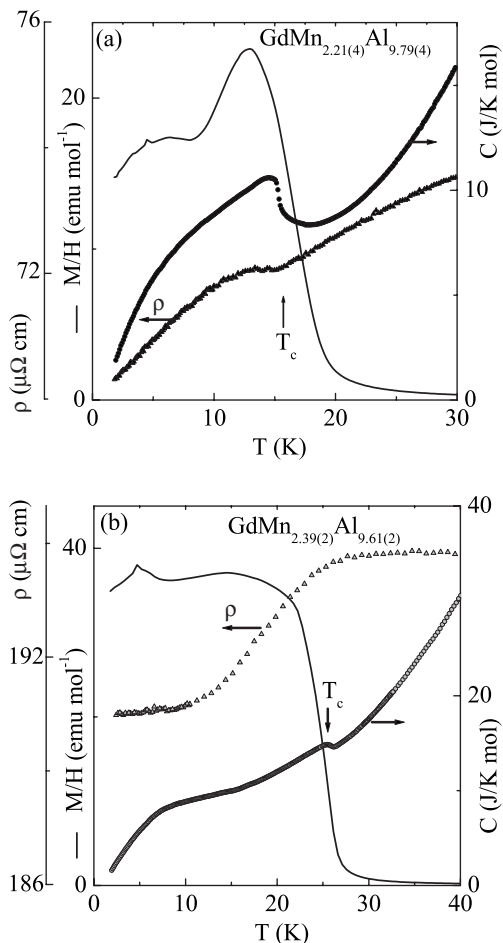


FIG. 16. For (a) $GdMn_{2.21(4)}Al_{9.79(4)}$ and (b) $GdMn_{2.39(2)}Al_{9.61(2)}$, temperature dependence of specific heat are shown along with resistivity and tetragonal average of magnetization by $M = [M_{\parallel c} + 2M_{\perp c}]/3$. The location of Curie temperature (T_c) for each is shown with a vertical arrow.

density of states.⁴⁰ For $LaMn_4Al_8$ with the nearest Mn-Mn interatomic distance of 2.58 Å [Fig. 2(a)], a small peak in magnetization at ~ 4.5 K is due to short-range correlations with $\mu_{\text{eff}} = 0.6\mu_B/\text{Mn}$.⁶

In $LaMn_{2+x}Al_{10-x}$, spin-glass behavior is found with the local magnetism, a result of excess Mn on the $Al3$ site (x). For $LaMn_{2.26(1)}Al_{9.74(1)}$ $\mu_{\text{eff}} \approx 5.8\mu_B/x\text{Mn}$ and for $LaMn_{2.41(3)}Al_{9.59(3)}$ $\mu_{\text{eff}} \approx 4.7\mu_B/x\text{Mn}$. The magnetic entropy released up to ~ 45 K is found to be $\sim 0.11R$ for 0.15(3) extra manganese. This means entropy of $\sim 0.8(2)R/\text{Mn}$, essentially within a factor of 2 of the expected $1.8R/\text{Mn}^{2+}$ or $1.6R/\text{Mn}^{3+}$. These results are consistent with local manganese moment on $Al3$ site.

For the $GdMn_{2+x}Al_{10-x}$ samples, ferromagnetic order is detected by a combination of magnetization, specific heat, and resistivity measurements (Fig. 16). The derived μ_{eff} values in the paramagnetic regions are those expected for Gd^{3+} free ion (Table V). For $GdMn_{2.21(4)}Al_{9.79(4)}$, there are 9(2)% intrachain Mn-Mn bond distances of 2.573(7) Å due to

excess Mn on Al3 site; for $\text{GdMn}_{2.39(2)}\text{Al}_{9.61(2)}$, there are 19(1)% of 2.570(4) Å intrachain bonds due to the partial occupancy of Mn on Al3. Given increasing x from a value of 0.21(4) ($T_C \approx 16$ K) to 0.39(2) ($T_C \approx 25.5$ K), it is reasonable to assume that there is a linear dependence between T_C and Mn concentration. If this is correct, then stoichiometric $\text{GdMn}_2\text{Al}_{10}$ should have $T_C \approx 5$ K.

ACKNOWLEDGMENTS

We are thankful to John D. Corbett for making single-crystal x-ray diffractometers available to us. We appreciate Josh Frederick's assistance with some of the sample preparations. Work at the Ames Laboratory was supported by the Department of Energy-Basic Energy Sciences under Contract No. DE-AC02-07CH11358.

- ¹V. M. T. Thiede and W. Jeitschko, *Z. Naturforsch* **53b**, 673 (1998).
- ²G. Cordier, E. Czech, H. Ochmann, and H. Schäfer, *J. Less-Common Met.* **99**, 173 (1984).
- ³P. J. Brown, B. Ouladdiaf, R. Ballou, J. Deportes, and A. S. Markosyan, *J. Phys.: Condens. Matter* **4**, 1103 (1992).
- ⁴J. Deportes and D. Givord, *Solid State Commun.* **19**, 845 (1976).
- ⁵I. H. Hagmusa, J. C. P. Klaasse, E. Bruck, F. R. De Boer, and K. H. J. Buschow, *J. Alloys Compd.* **297**, 21 (2000).
- ⁶T. Yamasaki, K. Matsui, H. Nakamura, and M. Shiga, *Solid State Commun.* **119**, 415 (2001).
- ⁷B. D. Rainford, C. J. Leavey, A. D. Hillier, and J. R. Stewart, *Physica B* **359-361**, 929 (2005).
- ⁸Y. Muro, S. Giri, G. Motoyama, H. Nakamura, and T. Kohara, *J. Phys. Soc. Jpn.* **74**, 1135 (2005).
- ⁹Y. Muro, G. Motoyama, H. Nakamura, and T. Kohara, *Physica B* **378-380**, 673 (2006).
- ¹⁰M. Coldea, M. Neumann, St. Lutkehoff, S. Mahl, and R. Coldea, *J. Alloys Compd.* **278**, 72 (1998).
- ¹¹I. Felner and I. Nowik, *J. Phys. Chem. Solids* **43**, 463 (1982).
- ¹²J. Deportes, D. Givord, R. Lemaire, and H. Nagai, *Physica B & C* **86-88**, 67 (1977).
- ¹³P. Schobinger-Papamantellos, P. Fischer, C. H. de Groot, F. R. de Boer, and K. H. J. Buschow, *J. Alloys Compd.* **232**, 154 (1996).
- ¹⁴N. P. Duong, J. C. P. Klaasse, E. Bruck, F. R. de Boer, and K. H. J. Buschow, *J. Alloys Compd.* **309**, L10 (2000).
- ¹⁵N. P. Duong, J. C. P. Klaasse, E. Bruck, F. R. de Boer, and K. H. J. Buschow, *J. Alloys Compd.* **315**, 28 (2001).
- ¹⁶R. Nirmala, V. Sankaranarayanan, K. Sethupathi, T. Geethkumary, M. C. Valsakumar, Y. Hariharan, and A. V. Morozkin, *Physica B* **329-333**, 673 (2003).
- ¹⁷P. G. De Gennes, *J. Phys. Radium* **23**, 510 (1962).
- ¹⁸E. Morosan, S. L. Bud'ko, and P. C. Canfield, *Phys. Rev. B* **72**, 014425 (2005).
- ¹⁹K. D. Myers, S. L. Bud'ko, I. R. Fisher, Z. Islam, H. Kleinke, A. H. Lacerda, and P. C. Canfield, *J. Magn. Magn. Mater.* **205**, 27 (1999).
- ²⁰S. L. Bud'ko, Z. Islam, T. A. Wiener, I. R. Fisher, A. H. Lacerda, and P. C. Canfield, *J. Magn. Magn. Mater.* **205**, 53 (1999).
- ²¹J. Mudryk, D. Fruchart, D. Gignoux, L. P. Romaka, and R. V. Skolozdra, *J. Alloys Compd.* **312**, 9 (2000); D. D. Jackson and Z. Fisk, *Phys. Rev. B* **73**, 024421 (2006).
- ²²P. C. Canfield and Z. Fisk, *Philos. Mag. B* **65**, 1117 (1992); P. C. Canfield and I. R. Fisher, *J. Cryst. Growth* **225**, 155 (2001).
- ²³IPDS II, Stoe and Cie GmbH, Darmstadt, Germany, 2002.
- ²⁴XSHAPE revision 2.03, crystal optimization for numerical absorption correction, Stoe and Cie GmbH, Darmstadt, Germany, 2003.
- ²⁵J. P. Glusker and K. N. Trueblood, *Crystal Structure Analysis*, 2nd ed. (Oxford University Press, New York, 1985).
- ²⁶SHELXTL, Bruker AXS, Inc., Madison, WI, 2000.
- ²⁷M. Angst, A. Kreyssig, Y. Janssen, J.-W. Kim, L. Tan, D. Wermeille, Y. Mozharivskiy, A. Kracher, A. I. Goldman, and P. C. Canfield, *Phys. Rev. B* **72**, 174407 (2005).
- ²⁸O. S. Zarechnyuk and P. I. Kripyakevich, *Kristallografiya* **7**, 543 (1962).
- ²⁹J. V. Florio, R. E. Rundle, and A. I. Snow, *Acta Crystallogr.* **5**, 449 (1952).
- ³⁰K. H. J. Buschow, J. H. N. van Vucht, and W. W. van der Hoogenhof, *J. Less-Common Met.* **50**, 145 (1976).
- ³¹J. Desportes, D. Givord, and K. Kebe, *J. Phys. C* **5-40**, 154 (1979).
- ³²K. Binder and A. P. Young, *Rev. Mod. Phys.* **58**, 801 (1986).
- ³³T. A. Wiener, I. R. Fisher, S. L. Bud'ko, A. Kracher, and P. C. Canfield, *Phys. Rev. B* **62**, 15056 (2000).
- ³⁴A. M. Palasyuk, B. Y. Kotur, E. Bauer, H. Michor, and G. Hilscher, *J. Alloys Compd.* **367**, 205 (2004).
- ³⁵I. Eremin, P. Thalmeier, P. Fulde, R. K. Kremer, K. Ahn, and A. Simon, *Phys. Rev. B* **64**, 064425 (2001).
- ³⁶K. Binder and A. P. Young, *Rev. Mod. Phys.* **58**, 801 (1986).
- ³⁷F. S. Liu, W. A. Roshen, and J. Ruvalds, *Phys. Rev. B* **36**, 492 (1987).
- ³⁸A. Arrott, *Phys. Rev.* **108**, 1394 (1957).
- ³⁹Y. Amako, H. Nagai, and K. Adachi, *J. Phys. Soc. Jpn.* **62**, 3355 (1993).
- ⁴⁰M. Shiga, *Physica B & C* **149**, 293 (1988).